D. Adair, et al., Int. J. Comp. Meth. and Exp. Meas., Vol. 7, No. 2 (2019) 106–117

THE INFLUENCE OF FINITE RUPTURE TIMES ON FLOW DYNAMICS WITHIN MICRO-SHOCK TUBES

DESMOND ADAIR[1], ABILKAIYR MUKHAMBETIYAR[1], MARTIN JAEGER[2] & MICHAEL MALIN[3]
[1] Department of Mechanical & Aerospace Engineering, Nazarbayev University, Astana, Kazakhstan.
[2] School of Engineering, University of Tasmania, Hobart, Australia.
[3] CHAM Ltd, Wimbledon Village, London, U.K.

ABSTRACT

The importance of micro-shock tubes is growing in line with recent developments of microscale technology for products like micro-heat engines and micro-propulsion systems. The flow dynamics within a micro-shock tube are different from those found in a macro shock tube, and knowledge of these dynamics is not as yet well established, as the flow within these tubes includes extra physics namely rarefaction and complex effects due to viscosity. Studies have recently been made with assumed initial condition of instantaneous diaphragm rupture producing centred shock and expansion waves. However, for a real case, the diaphragm ruptures over a finite time causing a period of partial rupture and this will change the shock characteristics. The work here reports on a series of axisymmetric numerical simulations carried out to calculate the influence of an initial finite-time diaphragm rupture. Rarefaction effects were taken into account by the use of Maxwell's slip velocity and temperature conditions. Use of an initial finite-time diaphragm rupture boundary condition causes the forming of a non-centred shock wave downstream of the diaphragm, and, the shock propagation distance is considerably reduced by use of the finite-time rupture process.

Keywords: CFD, finite rupture, micro-shock tube, Shock wave propagation, slip wall

1 INTRODUCTION

A shock tube generates a moving shock front by the sudden expansion of gas from a driver section (high pressure) into a driven section (low pressure). The moving shock front has accompanying expansion and contraction waves. Initially the driver and driven regions are separated by an impervious diaphragm which in turn bursts, with the subsequent formation of a moving shock wave which induces flow to move behind it. In contrast to macro tubes, micro-shock tubes show added flow physics, especially shock attenuation due to boundary layer growth and ensuing viscosity effects at low Reynolds numbers. When the Knudsen number is large, fluid near the wall slips because of non-continuum effects. This helps to grow shock strength and thereby increase wave propagation.

Within a micro-shock tube the viscous and rarefaction effects become much greater so giving simulations and experimental data of shock wave propagation and flow dynamics which are at odds with established theory [1]. This is primarily due to the pressure being low and the small geometry of the micro tube. To aid design and increase efficiency of devices based on a micro-shock tube, it is important to fully understand the shock wave propagation and related flow characteristics. Knowledge of the temperature characteristics of such devices may also be important.

The use of continuum-based simulations as opposed to molecular-based calculations is determined by the Knudsen number [2]. This is the ratio of mean-free-path to tube diameter. When the Knudsen number is low, less than 0.01, then the continuum-based simulations are appropriate. Between 0.01 and 0.1 Reynolds-averaged Navier-Stokes equations can be used with slip boundary conditions. Above 0.1 molecular calculation methods should be used.

Work involving macro tubes has already been carried out, for example by Duff [3] where the effect of boundary layer growth on shock propagation due to viscous loss was examined.

© 2019 WIT Press, www.witpress.com
ISSN: 2046-0546 (paper format), ISSN: 2046-0554 (online), http://www.witpress.com/journals
DOI: 10.2495/CMEM-V7-N2-106-117

Analytical modelling has been performed again investigating the effect of boundary layer growth on the shock propagation [4], together with the proposal of a scaling factor, S, which depends on the relationship of shock attenuation to tube diameter and initial pressure [5]. For low values of S in micro-shock tubes it has been calculated that the shock wave reduces greatly in strength due friction and heat conduction. Using a variety of boundary conditions good agreement was found between numerical calculations and analytical theory for calculations in the laminar region of the boundary layer [6]. Finally, the influence on shock propagation of wall friction and heat transfer has shown that shear stresses and energy losses close to the wall greatly affect the shock attenuation [7].

Unsteady Reynolds-averaged Navier-Stokes equations have been used in the calculation of flow within micro tubes [8], together with velocity slip and temperature jump equations. It was found that the shock wave strength decreased considerably for low initial pressures and small tube diameters. Other studies [9, 10] indicate that the forming of a boundary layer attenuates the shock wave propagation and, also by reducing the micro tube diameter, the shock strength greatly decays.

Studies in the last paragraph assume instantaneous opening of the diaphragm to produce a centred expansion and shock wave. However, in practice, a diaphragm bursts over a finite time and flow progresses in line with the available opening from the driver section to the driven section. Non-centred waves are produced in the driven section and the propagation characteristics are different to those of the sudden rupture process. The flow in the vicinity of the diaphragm becomes very complex. The question arises as to how to simulate the actual diaphragm rupture. Hickman *et al.* [11] proposed that the diaphragm initially bulges and that the opening starts at the diaphragm centre. Later Outa *et al.* [12] proposed a cosine opening function with respect to time and recently Matsuo *et al.* [13] proposed a quadratic function.

In the current work a 2D axisymmetric CFD approach was used to simulate unsteady flow evolvement and shock propagation inside a micro-shock tube. The optimal mathematical function to describe the finite-time rupture of the diaphragm was established followed by a comparison of the characteristics found in the driven section between gradual and sudden diaphragm rupture.

2 MICRO-SHOCK TUBE (COMPUTATIONAL DOMAIN)

A micro-shock tube consists of a driver region, a driven region and a diaphragm initially used as separator as can be seen from Fig. 1. Initially high pressure and low pressure are assigned to the driver and driven regions, respectively. When the diaphragm is ruptured, a moving shock wave front develops due to the pressure difference. Reflection of the shock wave occurs when it meets the solid end-wall of the driver region.

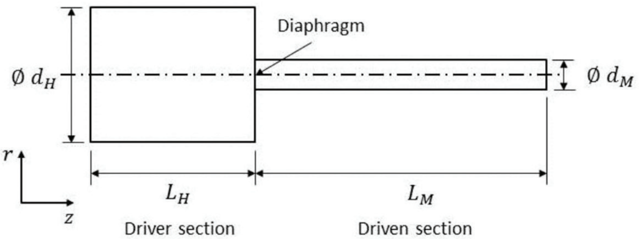

Figure 1: Closed micro-shock tube.

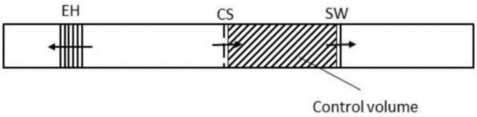

Figure 2: Terminology associated with shock front.

In this work the dimensions (L_H) and (L_M) for the driver and driven regions were 41mm and 66mm respectively while the equivalent diameters (d_H) and (d_M) were 20mm and 7.5mm.

Some helpful terminology regarding a shock front travelling along the driven section is shown in Fig. 2. EH, CS and SW respectively represent expansion head, contact surface and shock wave.

3 NUMERICAL CALCULATIONS

3.1 Governing equations

Two-dimensional, axisymmetric, transient, calculations were made using Reynolds-averaged compressible Navier-Stokes equations coupled with the energy equation. The conservation equations used were

Continuity

$$\frac{\partial \rho}{\partial t}+\frac{1}{r}\frac{\partial(r\rho u)}{\partial r}+\frac{\partial(\rho w)}{\partial z}=0, \tag{1}$$

Axial Momentum

$$\begin{aligned}\frac{\partial(\rho w)}{\partial t}+\frac{1}{r}\frac{\partial(r\rho ww)}{\partial z}+\frac{1}{r}\frac{\partial(r\rho uw)}{\partial r}&=-\frac{\partial p}{\partial z}\\&+\frac{1}{r}\frac{\partial}{\partial z}\left[r\mu(2\frac{\partial w}{\partial z}-\frac{2}{3}(\nabla\cdot\vec{v})\right]+\frac{1}{r}\frac{\partial}{\partial r}\left[r\mu\left(\frac{\partial w}{\partial r}+\frac{\partial u}{\partial z}\right)\right]+F_z,\end{aligned} \tag{2}$$

Radial Momentum

$$\begin{aligned}\frac{\partial(\rho u)}{\partial t}+\frac{1}{r}\frac{\partial(r\rho wu)}{\partial z}+\frac{1}{r}\frac{\partial(r\rho uu)}{\partial r}&=-\frac{\partial p}{\partial r}+\frac{1}{r}\frac{\partial}{\partial z}\left[r\mu\left(\frac{\partial u}{\partial z}+\frac{\partial w}{\partial r}\right)\right]\\&+\frac{1}{r}\frac{\partial}{\partial r}\left[r\mu\left(2\frac{\partial u}{\partial r}-\frac{2}{3}(\nabla\cdot\vec{v})\right)\right]-2\mu\frac{u}{r^2}+\frac{2}{3}\frac{\mu}{r}(\nabla\cdot\vec{v})+F_r,\end{aligned} \tag{3}$$

Energy

$$\begin{aligned}\frac{\partial(\rho e)}{\partial t}+\frac{1}{r}\frac{\partial(r\rho hu)}{\partial r}+\frac{1}{r}\frac{\partial(\rho hw)}{\partial z}&=\frac{\partial u}{\partial r}\left(2\mu\frac{\partial u}{\partial r}-\frac{2}{3}\mu(\nabla\cdot\vec{v})\right)\\+u\left(\frac{2}{3}\frac{(2\mu u-r\mu(\nabla\cdot\vec{v})}{r^2}\right)&+\frac{\partial w}{\partial z}\left(2\mu\frac{\partial w}{\partial z}-\frac{2}{3}\mu(\nabla\cdot\vec{v})\right)+\mu\left(\frac{\partial u}{\partial z}+\frac{\partial w}{\partial r}\right)^2\end{aligned} \tag{4}$$

$$+u\left(\frac{1}{r}\frac{\partial}{\partial r}\left(\left(2\mu\frac{\partial u}{\partial r}-\frac{2}{3}\mu\left(\nabla\cdot\vec{v}\right)\right)\right)-\frac{2}{3}\frac{\left(2\mu u-r\mu\left(\nabla\cdot\vec{v}\right)\right)}{r^{2}}+\frac{\partial}{\partial z}\left(\mu\left(\frac{\partial u}{\partial z}+\frac{\partial w}{\partial r}\right)\right)\right)$$

$$+w\left(\frac{1}{r}\frac{\partial}{\partial r}\left(r\mu\left(\frac{\partial u}{\partial z}+\frac{\partial w}{\partial r}\right)\right)+\frac{\partial}{\partial z}\left(2\mu\frac{\partial w}{\partial z}-\frac{2}{3}\mu\left(\nabla\cdot\vec{v}\right)\right)\right)-\frac{1}{r}\frac{\partial\left(rq_{r}\right)}{\partial r}-\frac{\partial q_{z}}{\partial z},$$

where

$$\nabla\vec{v}=\frac{\partial w}{\partial z}+\frac{\partial u}{\partial r}+\frac{u}{r}. \tag{5}$$

In the above, the radial and axial coordinates are r and z respectively, and the radial and axial velocities are u and w respectively. The static pressure is p, h is enthalpy and μ is molecular viscosity. F is body force and q_r and q_z are the radial and axial heat fluxes respectively.

The total energy per unit mass (e) in the above equations is evaluated as

$$e=h-p/\rho. \tag{6}$$

The PHOENICS-2018 [14] code together with some additional coding inserted using the In-Form facility found in PHOENICS was used for the computation of these equations. In order to calculate density, the ideal gas law was used and to discretize convection the higher-order van Lee MUSCL scheme was chosen. A first-order Euler scheme was used for time-stepping. When appropriate, i.e. at very low pressure during rarefaction, the Maxwell slip velocity and jump equations [2] were used in the near wall region as

$$w_{w}-w_{g}=\left(\frac{2-\alpha_{v}}{\alpha_{v}}\right)\frac{\lambda}{\delta}\left(w_{g}-w_{c}\right), \tag{7}$$

$$T_{s}-T_{w}=2\left(\frac{2-\alpha_{T}}{\alpha_{T}}\right)\frac{\lambda}{\delta}\left(T_{g}-T_{c}\right), \tag{8}$$

$$\lambda=\frac{k_{B}T}{\sqrt{2}\pi\sigma^{2}p}. \tag{9}$$

Here k_B is Boltzmann's constant, σ is the Lennard-Jones characteristic length. The α coefficents are momentum and thermal accommodations, the mean free path is λ and δ is the distance from the wall. The subscripts g, w and c refer to gas, wall and cell-centre. The slip velocity was derived from Eq. (7).

The viscosity was modelled using the Sutherland viscosity model and is a function of temperature

$$\mu=\mu_{0}\left(\frac{T}{T_{0}}\right)^{1/2}\frac{T_{0}+S_{u}}{T+S_{u}}. \tag{10}$$

In Eq. (10) the viscosity of the gas is μ, with μ_0 a reference viscosity, The temperature is T, with T_0 a reference temperature. S_u is the Sutherland constant.

3.2 Computational domain

The computational domain was discretized using a structured, cylinder-polar mesh. Grid independence was tested with the final mesh size chosen as 120 radial by 1200 axial cells. The numbers in the driven region was 60 radial by 720 axial cells, and in the driver region 120 radial by 480 axial cells. Close to solid walls and the diaphragm region refinement of the mesh was achieved using geometric progression. This is shown in Fig. 3 where only some of the mesh has been selected to give clarity.

Each calculation was run for 0.3ms using uniform time steps detailed in Table 1. The k-ω SST turbulence model [15, 16] mentioned in Table 1 is a two-equation eddy-viscosity model. The use of a k-ω formulation in the inner parts of the boundary layer makes the model directly useable down to the viscous sub-layer. The SST formulation switches to a k-ε behaviour in the free-stream. It was found not to be necessary to use under-relaxation and the convergence criteria for each variable was 10^{-4}. The computer was a Dell 5500 Workstation with an Intel Xeon Six Core Processor (2.66 GHz) with 16GB RAM.

3.3 Validation

The calculation method, using instantaneous diaphragm rupture, was tested by comparing with an analytical solution and experimental results. 1D transient calculations were made and compared with an analytical solution [17] for macro shock flow. It is appropriate to test the calculation method against macro shock tube flow as shock waves, contact discontinuity and rarefaction waves are common to both macro- and micro-shock tubes. The macro tube chosen for this part of the validation was 10m long and had a cross-sectional area of 0.1m^2. During the calculations, 90 cells were used in the computational domain. For the driver section initial

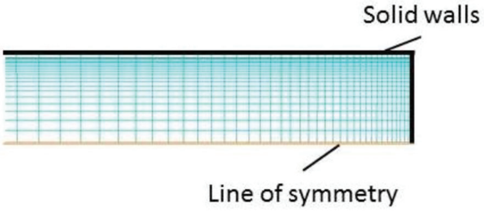

Figure 3: Refinement of the grid close to solid surfaces.

Table 1: Computation specifics

Energy equation	Enthalpy (h)
Time step	0.1 μs
Grid arrangement	Staggered
Turbulence model	k-ω SST
Solution algorithm	Implicit SIMPLEST
Time differencing	1st Order Euler
Discretization	MUSCL
Elapsed run-time (0.2ms)	20.0 hours

pressure was set at 1bar, the temperature 348.391K and the density of the gas 1.0kg/m^3. For the driven section the initial pressure was set at 0.1bar, the temperature 278.13K and the density of the gas 0.125kg/m^3. The boundary condition for the wall was non-slip and the energy equation was solved as enthalpy using the ideal gas law. For the discretization of convection the higher-order Van Leer MUSL scheme was used. As shown in Fig. 4 quite good agreement was found for the axial temperature distribution between the analytical solution and the calculations, with the results within the shock in good agreement. However, just at the start and finish of the shock, the temperature was not calculated very accurately. This may be due to the MUSCL scheme used, so in an attempt to rectify this deficiency, the suggestions due to Suresh and Huynh [18] for the necessity to satisfy the monotonicity by the enlargement of the TVD intervals were introduced. A slight improvement in the calculation of the variables towards the shock ends resulted as can be seem for the temperature distribution in Fig. 4.

A second validation was made by comparison of calculations with the experimental results of Park *et al.* [19] who used a micro-shock tube of 6mm diameter with a pressure ratio (Pr) of 6. The driven section was initially set at 1atm. The calculated shock- and expansion-wave propagation curves are shown in Fig. 5. Here EH and SW represent the expansion head and shock wave respectively.

There is quite good agreement between the experimental and calculated results although less attenuation is found from the calculations. This could be because real gas flow is more

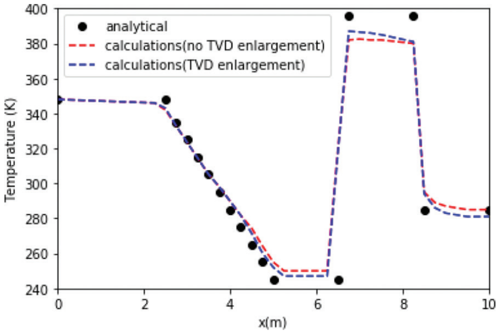

Figure 4: Comparison of calculated results with measurements in a macro shock tube.

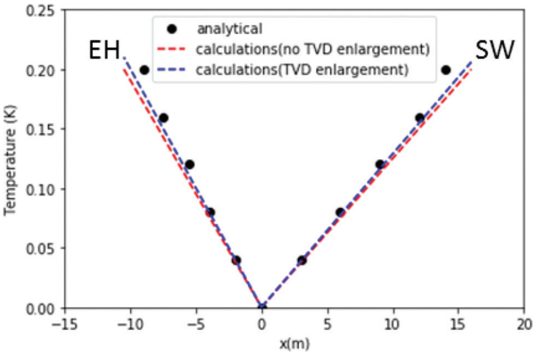

Figure 5: Experimental and calculated results for wave location at different times.

viscous and there is heat transfer from the shock-heated gas to the walls of the shock tube. The boundary conditions used at the walls were adiabatic with the fixed value 300K. Again the inclusion of TVD enlargement helps to improve the calculations a little.

3.4 Finite rupture-time modelling

It is important to describe first the mechanics of how the diaphragm in the present work ruptures. It has been previously postulated and proven [20] that left to its own devices a cellophane diaphragm will most likely rupture first around its periphery due to dynamic pressure loading. However this is not the scenario considered here. Rather, to coincide with experimental data it will be assumed in all the present work that initial rupture occurs at the centre-line of the tube induced with the aid of a needle [13].

To reproduce the bursting of the diaphragm with respect to time, three functions were investigated, namely linear, quadratic and square-root

Linear $$r = \alpha t, \tag{11}$$

Quadratic $$r = \beta t^2, \tag{12}$$

Square-root $$r = \gamma \sqrt{t}. \tag{13}$$

where r is the opened radius at the arbitrary time t, α is the constant R / T, where R is the total tube radius and T is the total time to open fully, $\beta = R / T^2$, and $\gamma = R / \sqrt{T}$. To find which of these functions is the most suitable representation of the finite-time diaphragm rupture, calculations were made using the geometry of [13] which was a tube of 65.5mm diameter with a pressure ratio of $P_4 / P_1 = 2$ where P_4 is the initial pressure of the driver domain and P_1 is the initial pressure of the driven domain. From the experiment [10] it was shown that the total rupture time was approximately $T = 0.216$ms with P_4 set at 101,325Pa. Figure 6 compares the diaphragm opening radius r for the different functions described by Eqns. (11–13) and it can be clearly seen that the rupture progresses initially much slower for the linear and quadratic functions when compared to the square-root function.

If a direct relationship of diaphragm rupture time with area is assumed then the rupture time for different shock tube diameters can be inferred. For a tube of diameter 7.5mm the time of rupture was found as approximately 3μ.

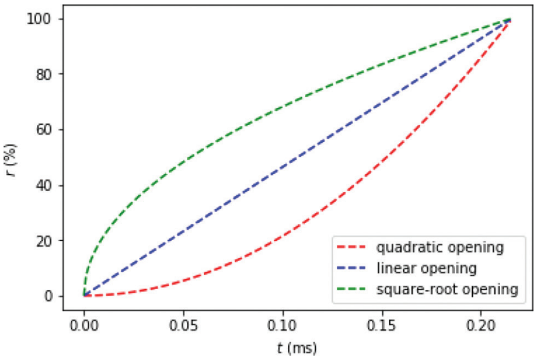

Figure 6: Diaphragm opening radius for different time functions.

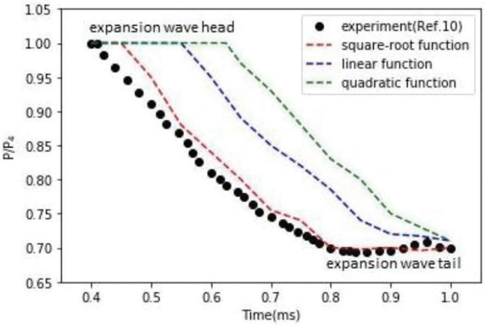

Figure 7: Pressure history for different time functions at $\frac{x}{D} = -2.29$.

Half of the diaphragm was discretized into 30 sub-divisions which coincided with 30 discrete time steps, and initially the diaphragm sub-divisions were considered to be solid and impervious, and, at each time step, an additional sub-division was opened. The sub-division lengths were set according to which opening time function was in use. In the experiment, the diaphragm bursts in a continuous fashion but it was considered here that 30 time steps were sufficient to represent the continuous functions of Fig. 6.

Figure 7 shows the variation of static pressure at the experimental measuring point for different initial time functions.

It is clear that the square-root function is much closer to the experimental results showing that the rupture process is initially fast and gradually slows. Due to these encouraging results all finite-time diaphragm rupture calculations made in the rest of this paper use a square-root function for the total diaphragm opening time.

4 RESULTS AND DISCUSSION

Comparison is now made between characteristics of the resultant flow for gradual and sudden rupture of the diaphragm. Extensive calculations have already been reported for a sudden rupture of the diaphragm [9] using the computational domain shown in Fig. 1. The initial conditions chosen for comparison were, $P_4 / P_1 = 9$, $P_1 = 101325\text{Pa}$, the Knudsen number (Kn) for the driven section set at 9×10^{-6} and the initial temperature (T) set at 300K. The wall boundary condition was non-slip.

For gradual diaphragm rupture the flow evolvement into the driven region gradually takes place leading to several compression waves being formed which eventually coalesce leading to a shock wave being formed. The flow evolvement at the end of the gradual rupture period is shown in Fig. 8 and is represented using temperature contours. The development of the contact surface (CS) and shock wave (SW) are seen by the increase and fall of the temperature values. Shown in Fig. 9 is the development of the shock front for times during the gradual diaphragm rupture period.

Because of finite time to achieve full rupture, it takes time for flow into the driven section to fully develop. Therefore the full shock front also takes time to form and will start downstream of the diaphragm, as opposed to instantaneous rupture where the shock wave forms immediately. A good indication of the shock strength is the temperature ratio across the shock, T_2 / T_1. The analytical solution (inviscid) gives the temperature ratio as a constant and higher value than the solution here due to the constant attenuation of shock strength

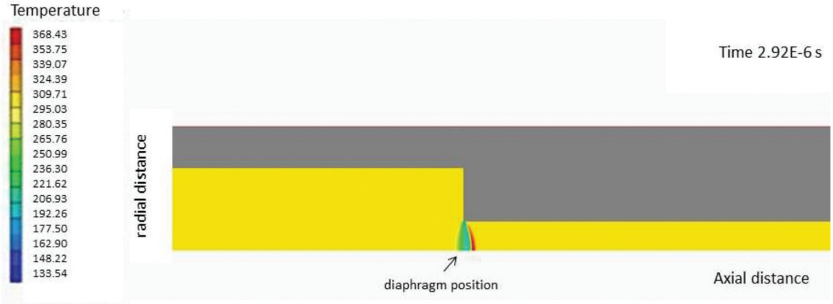

Figure 8: Temperature distributions in the diaphragm region at the end of the gradual diaphragm rupture.

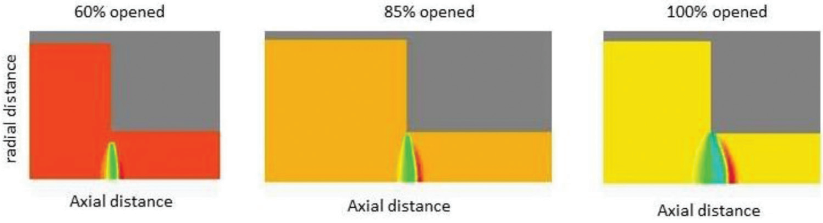

Figure 9: Temperature contours in the vicinity of the diaphragm during the rupture progression

due to viscous losses. The progression of the shock strength with time during and after gradual rupture is shown in Fig. 10, which also explains the formation distance of the shock front.

The distance between shock and contact variation is given in Fig. 11. It can be seen that the resulting shock-contact distance is strongly dependent on the initial assumption of diaphragm rupture, i.e. the gradual diaphragm opening gives a much reduced shock speed and hence a shorter shock-contact distance results when compared to the instantaneous diaphragm bursting process.

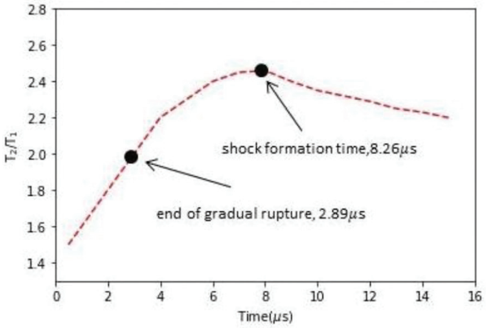

Figure 10: Temperature ratio distribution indicating the strength of the shock wave travelling along the driven region with time.

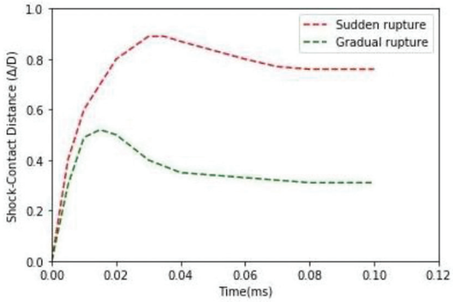

Figure 11: Shock-contact distance variation for instantaneous and gradual diaphragm ruptures.

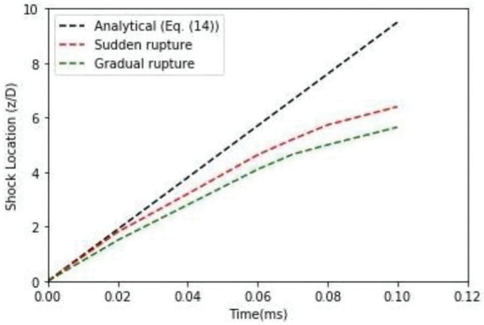

Figure 12: Location of the shock front along centre-line in the driven section for sudden and gradual ruptures.

A shock wave resulting from a burst diaphragm moves within a driven region with a Mach number M_S. In an ideal micro-shock tube, with fixed initial conditions, M_S can be calculated from

$$\frac{P_4}{P_1} = \left\{1 + \frac{2\gamma_1}{\gamma_1 + 1}\left(\mathrm{M}_S^2 - 1\right)\right\}\left\{1 - \frac{\gamma_4 - 1}{\gamma_4 + 1}\frac{\alpha_1}{\alpha_4}\left(\mathrm{M}_S - \frac{1}{\mathrm{M}_S}\right)\right\}^{-2\gamma_4 / \gamma_4 - 1} . \tag{14}$$

where γ is the mean free path and is a function of the Boltzmann constant, the Lennard-Jones characteristic length of species, temperature and pressure. The Mach number keeps constant in a given micro-shock tube [1]. It is shown in Fig. 12 that the shock front location for the gradual rupture lags behind that of the instantaneous rupture. The analytical ideal inviscid solution as given by Eq. (14) where the theoretical Mach number M_S was set at 2.1 is seen to over-predict the shock front speed when compared to the other two solutions.

CONCLUSIONS

In this work the effect of having a gradual opening of the diaphragm instead of an initial instantaneous rupture of the diaphragm was studied. It was found that the gradual rupture of the diaphragm leads to a gradual flow progression over the time of rupture. Compression waves develop which coalesce and eventually form a moving shock front, and, as such the full shock front starts downstream of the diaphragm and not, as with the instantaneous opening, at the diaphragm location. The time of rupture was found to be very small and the best function describing the opening process was found to be the square-root function. The shock propagation distance for the gradual rupture case was found to be less than that for the instantaneous rupture case.

REFERENCES

[1] Zhang, G., Setoguchi, T. & Kim, H.D., Numerical simulation of flow characteristics to micro shock tubes. *Journal of Thermal Science*, **24**(3), pp. 246–253, 2015. https://doi.org/10.1007/s11630-015-0780-4

[2] Karniadakis, G.E.M. & Beskok, A., *Micro Flows Fundamentals and Simulation*, Springer, New York, 2002.

[3] Duff, R.E., Shock tube performance at initial low pressure. *Physics of Fluids*, **2**, pp. 207–216, 1959. https://doi.org/10.1063/1.1705910

[4] Mirels, H., Test time in low pressure shock tube. *Physics of Fluids*, **6**, pp. 1201–1214, 1963. https://doi.org/10.1063/1.1706887

[5] Brouillete, M., Shock waves at microscales. *Shock Waves*, **13**, pp. 3–12, 2003. https://doi.org/10.1007/s00193-003-0191-4

[6] Kohsuke, T., Kazuaki, I. & Makoto, Y., Numerical investigation on transition of shock induced boundary, *47th AIAA Aerospace Meeting including the New Horizons Forum and Aerospace Exposition*, Orlando, Florida, 2009.

[7] Ngomo, D., Chaudhuri, D., Chinnayya, A. & Hadjadj, A., Numerical study of shock propagation and attenuation in narrow tubes including friction and heat losses. *Computers & Fluids*, **39**, pp. 1711–1721, 2010. https://doi.org/10.1016/j.compfluid.2010.06.005

[8] Zeitoun, D.E., Burtschell, Y. & Graur, I.A., Numerical simulation of shock wave propogation in micro channels using continuum and kinetic approaches. *Shock Waves*, **19**, pp. 307–316, 2009. https://doi.org/10.1007/s00193-009-0202-1

[9] Mukhambetiyar, A., Jaeger, M. & Adair, D., CFD modelling of flow characteristics in micro shock tubes. *Journal of Applied Fluid Mechanics*, **10**(4), pp. 1061–1070, 2017. https://doi.org/10.18869/acadpub.jafm.73.241.27474

[10] Arun, K.R. & Kim, H.D., Computational study of the unsteady flow characteristics of a micro shock tube. *Journal of Mechanical Science and Technology*, **27**(2), pp. 451–459, 2012. https://doi.org/10.1007/s12206-012-1259-9

[11] Hickman, R.S., Farrar, L.C. & Kyser, J.B., Behaviour of burst diaphragms in shock tubes. *Physics of Fluids*, **18**(10), pp. 1249–1252, 1975. https://doi.org/10.1063/1.861010

[12] Outa, E., Tajima, K. & Hayakawa, K., Shock tube flow influenced by diaphragm opening (two-dimensional flow near the diaphragm), *10th International Symposium on Shock Waves and Shock Tubes*, Kyoto, Japan, 14–16 July, 1975.

[13] Matsuo, S., Mohammad, M., Nakano, S. & Kim, H.D., Effect of diaphragm rupture process on flow characteristics in a shock tube using dried cellophane, *Proceedings*

of the International Conference on Mechanical Engineering (ICME), Dhaka, 29–31 December, 2007.

[14] Cham Ltd., PHOENICS CODE 2018, Cham Ltd., Wimbledon, London, UK.

[15] Menter, F.R., Zonal two equation k-ω turbulence models for aerodynamic flows. *AIAA Paper* 93-2906, 1993.

[16] Menter, F.R., Two-equation eddy-viscosity turbulence models for engineering applications. *AIAA Journal*, **32**(8), pp. 1598–1605, 1994. https://doi.org/10.2514/3.12149

[17] Sod, G.A., A survey of several finite difference methods for systems on nonlinear hyperbolic conservation laws. *Journal of Computational Physics*, **27**, pp. 1–13, 1978. https://doi.org/10.1016/0021-9991(78)90023-2

[18] Suresh, A. & Huynh, H.T., Accurate monotonicity-preserving schemes with Runge-Kutta time stepping. *Journal of Computational Physics*, **136**, pp. 83–99, 1997. https://doi.org/10.1006/jcph.1997.5745

[19] Park, J.O., Kim, G.W. & Kim, H.D., Experimental study of the shock wave dynamics in micro shock tube. *Journal of the Korean Society of Propulsion Engineers*, **17**(5), pp. 54–59, 2014. https://doi.org/10.6108/kspe.2013.17.5.054

[20] Wegener, M., Sutcliffe, M. & Morgan, R., Optical study of a light diaphragm rupture process in an expansion tube. *Shock Waves*, **10**, pp. 167–178, 2000. https://doi.org/10.1007/s001930050003